Check for updates

AGU ADVANCING EARTH AND SPACE SCIENCES

Water Resources Research

RESEARCH ARTICLE
10.1029/2024WR037427

Influence of Evaporation and High-Frequency Seawater Inundation on Salinity Dynamics in Swash Zones

Xiaolong Geng[1,2], Holly A. Michael[3,4], James W. Heiss[5], Michel C. Boufadel[6], Hailong Li[7], and Xuejing Wang[8]

[1]Department of Earth Sciences, University of Hawai'i at Mānoa, Honolulu, HI, USA, [2]Water Resources Research Center, University of Hawai'i at Mānoa, Honolulu, HI, USA, [3]Department of Earth Sciences, University of Delaware, Newark, DE, USA, [4]Department of Civil and Environmental Engineering, University of Delaware, Newark, DE, USA, [5]Department of Environmental, Earth, and Atmospheric Sciences, University of Massachusetts - Lowell, Lowell, MA, USA, [6]Department of Civil and Environmental Engineering, New Jersey Institute of Technology, University Heights, Newark, NJ, USA, [7]State Environmental Protection Key Laboratory of Integrated Surface Water-Groundwater Pollution Control, School of Environmental Science & Engineering, Southern University of Science and Technology, Shenzhen, China, [8]Institute of Surface-Earth System Science, School of Earth System Science, Tianjin University, Tianjin, China

Key Points:

- Waves generate a saline plume beneath the swash zone with hypersalinity triggered by evaporation
- Swash motion increases surface moisture and evaporation rate, with high-frequency fluctuations caused by waves occurring in both
- Optimal hydrogeological and atmospheric conditions interact to maximize salt accumulation at the swash zone through evaporation

Supporting Information:

Supporting Information may be found in the online version of this article.

Correspondence to:

X. Geng,
gengxiaolong@gmail.com

Citation:

Geng, X., Michael, H. A., Heiss, J. W., Boufadel, M. C., Li, H., & Wang, X. (2024). Influence of evaporation and high-frequency seawater inundation on salinity dynamics in swash zones. *Water Resources Research*, *60*, e2024WR037427. https://doi.org/10.1029/2024WR037427

Received 29 FEB 2024
Accepted 16 OCT 2024

© 2024. The Author(s).
This is an open access article under the terms of the Creative Commons Attribution License, which permits use, distribution and reproduction in any medium, provided the original work is properly cited.

Abstract The interactions between the atmosphere, ocean, and beach in the swash zone are dynamic, influencing water flux and solute exchange across the land-sea interface. This study employs groundwater simulations to examine the combined effects of waves and evaporation on subsurface flow and salinity dynamics in a shallow beach environment. Our simulations reveal that wave motion generates a saline plume beneath the swash zone, where evaporation induces hypersalinity near the sand surface. This leads to the formation of a hypersaline plume beneath the swash zone during periods of wave recession, which extends vertically downward to a maximum depth of 30 cm, driven by the resulting vertical density gradients. This hypersaline plume moves approximately 2 m landward to the top of the swash zone and down the beachface due to wave-induced seawater infiltration and is subsequently diluted by the surrounding saline groundwater. Furthermore, swash motion increases near-surface moisture, leading to an elevated evaporation rate, with dynamic fluctuations in both moisture and evaporation rate due to high-frequency surface inundation caused by individual waves. Notably, the highest evaporation rates on the swash zone surface do not always correspond to the greatest elevations of salt concentration within the swash zone. This is because optimal moisture is also required—neither too low to impede evaporation nor too high to dilute accumulated salt near the surface. These insights are crucial for enhancing our understanding of coastal groundwater flow, biogeochemical conditions, and the subsequent nutrient cycling and contaminant transport in coastal zones.

Plain Language Summary The interactions between the atmosphere, ocean, and beach in the swash zone on beaches complicate movement of water and salt across the land-sea interface. Our results, for the first time, demonstrate that wave motion and evaporation cause high salinity water to accumulate just beneath the sand surface. The saline water expands during periods of wave recession and diminishes when waves become strong again. These insights highlight the necessity of considering integrated coastal physical drivers when investigating coastal flow and transport processes in swash zones, which have strong implications for coastal biogeochemical processes and ecosystems.

1. Introduction

The swash zone is widely recognized as a reactive zone where various biogeochemical processes occur, including the cycling and transformation of elements such as carbon, nutrients (e.g., N, P, and S), and metals (e.g., Fe and Mn) in foreshore beach sediments (Cockcroft, 1990; Morgan et al., 2018; Uchiyama et al., 2000; Wang et al., 2017). This zone is characterized by high-frequency inundation and seawater infiltration driven by individual waves, resulting in dynamic seawater-groundwater exchange and salinity fluctuations (Geng et al., 2017, 2020; Heiss et al., 2015; Horn, 2006; Sous et al., 2016). Previous studies have shown that the mixing of seawater and fresh groundwater plays a critical role in shaping near-shore microbial communities and their activities related to primary productivity and decomposition in coastal beach aquifers (Mouret et al., 2020). In particular, salinity levels impact the spatial and seasonal distribution patterns of microorganisms in coastal regions (Chambers et al., 2016; Lew et al., 2022; Zeppilli et al., 2018). Elevated interstitial salinity has been linked to increased emergence rates for certain species such as Platyhelminthes and Copepod (Armonies, 1988; Zeppilli

19447973, 2024, 11, Downloaded from https://agupubs.onlinelibrary.wiley.com/doi/10.1029/2024WR037427, Wiley Online Library on [26/11/2024]. See the Terms and Conditions (https://onlinelibrary.wiley.com/terms-and-conditions) on Wiley Online Library for rules of use; OA articles are governed by the applicable Creative Commons License

et al., 2018). Hypersaline conditions have been identified as a critical limiting factor for the microbial degradation of oil in Gulf of Mexico beaches following the Deepwater Horizon oil spill (Abou Khalil et al., 2020; Geng, Khalil, et al., 2021). Furthermore, the mixing dynamics in the swash zone influence terrestrial chemical fluxes entering coastal waters through submarine groundwater discharge (Charbonnier et al., 2013; Kim & Heiss, 2021; Moore & Joye, 2021). Therefore, characterizing groundwater flow and salinity dynamics in the swash zone and the physical parameters that influence these dynamics is crucial for understanding the role of swash zones in regulating biogeochemical transformations and associated chemical loads in the coastal zone.

Over the past four decades, numerous studies have investigated groundwater mixing dynamics in response to swash motions in coastal zones (e.g., Geng & Boufadel, 2015a, 2015b, 2015c; Geng et al., 2020; Longuet-Higgins & Smith, 1983; Robinson et al., 2014; Sous et al., 2016). Laboratory experiments have revealed that waves create steep hydraulic gradients, forming a saline groundwater circulation cell beneath the beach surface that extends from the lower end of the swash zone to the surf zone (Longuet-Higgins, 1983; Sous et al., 2013; Steenhauer et al., 2011; Turner et al., 2016). This circulation cell affects the transport pathways and transit time of inland-derived solutes in the beach before discharge (Anwar et al., 2014; Boufadel et al., 2007). Wave studies have also been carried out in the field to investigate moisture and flow dynamics in beach systems in response to high-frequency wave motions (Atherton et al., 2001; Heiss et al., 2014, 2015; Sous et al., 2016). These studies observed the presence of a consistent groundwater circulation pattern under the swash zone. Additionally, the studies demonstrated that the lens of infiltrating seawater, which moves downward through the unsaturated zone to the water table and contributes to the formation of the circulation cell, moves landward and seaward as the tide and swash zone move across the beach surface (e.g., Heiss et al., 2020).

Numerical modeling has been recognized as an effective tool to characterize swash zone dynamics (Geng, Heiss, et al., 2021; Horn, 2006; Huizer et al., 2017). Phase-resolving modeling of surface waves includes the explicit reproduction of the sea surface and velocity field evolution. This approach is often computationally expensive due to the coupling turbulence models (e.g., k–ε model, k–ω model, and Reynold stress equation model) and volume of fluid (VOF) techniques (Hirt & Nichols, 1981; Wilcox, 1993, 1998). Studies have incorporated phase-resolving modeling of waves into groundwater simulations (Bakhtyar et al., 2011; Geng et al., 2014). Site-specific modeling has also been conducted, where high-frequency wave-induced pressure oscillations along the beach surface were measured and adopted for groundwater simulations (Geng et al., 2017, 2020). To improve numerical efficiency, approaches have been developed to upscale the impacts of waves on groundwater flow and solute transport in beach aquifers (Geng & Boufadel, 2015b; Robinson et al., 2014; Xin et al., 2010). In these approaches, wave effects are represented either by the shallow-water equation (Steenhauer et al., 2011), or a wave-induced onshore hydraulic gradient above the mean sea level, referred to as wave setup (Xin et al., 2010), or spatially varying infiltration rates along the beach surface averaged over several wave periods (Geng & Boufadel, 2015b). While these aforementioned upscaling approaches significantly reduce computational costs, they cannot capture the high-frequency oscillations of subsurface flow and moisture content in response to swash motions. However, resolving the high-frequency oscillations is required for modeling and understanding other physical processes tied to wave runup and rundown, such as evaporation from the swash zone surface (Figure 1).

Evaporation plays a pivotal role in hydrologic cycles, impacting subsurface flow and transport processes in aquifers (Li et al., 2005; Silvestri et al., 2005; Zhang et al., 2014). Prior research showed that evaporation at the land surface leads to upwelling of groundwater (Geng & Boufadel, 2015a). Along coastal areas, evaporation leads to the accumulation of salt near the sediment surface (Geng & Boufadel, 2015c; Geng et al., 2016). As salt accumulates at the surface, it generates vertical density gradients that can cause pore water to flow downward. These opposing driving forces, evaporation and the resulting vertical density gradient, create a complex mechanism influencing subsurface flow and salt transport in beach aquifers (Geng & Boufadel, 2017). Coastal beach systems typically feature a shallow groundwater table, resulting in relatively high water content near the surface. The rate of evaporation from the ground surface depends on the humidity gradient between the air and land surface. Therefore, a high water content near the beach surface facilitates the evaporation of pore water from the sediments (Mahfouf & Noilhan, 1991; Xin et al., 2017). The shallow groundwater table also establishes a strong hydraulic connection between the evaporation front and deep groundwater, effectively replenishing the water lost to evaporation from the surface and leading to a sustainable evaporation rate (Liu et al., 2022). Furthermore, our recent study revealed that evaporation-induced upwelling of groundwater can facilitate the migration of solutes from deep sediments to the surface (Geng et al., 2023).

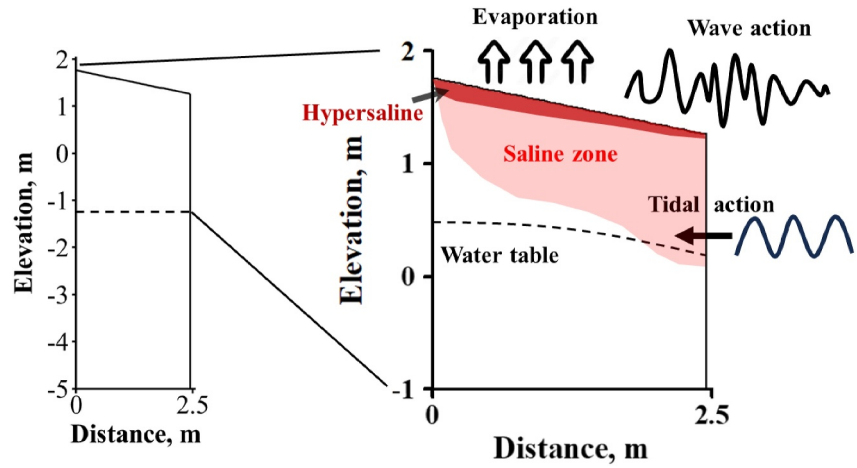

Figure 1. Model domain and conceptual model of salinization process in swash zone influenced by tides, waves, and evaporation. The elevation is referenced relative to mean sea level.

Within the swash zone, wave-induced periodic inundation results in seawater infiltrating into the beach, salinizing near-surface sediments. Subsequent exposure of these sediments to the atmosphere allows evaporation to regulate flow and accumulate salt beneath the swash zone (Figure 1). The interaction of wave motions with evaporation may induce a complex driving mechanism that governs groundwater flow and the transport of solutes/contaminants in the swash zone. This modulating mechanism is expected to be more pronounced in beaches with high moisture and shallow groundwater tables due to a strong hydraulic connection between the near-surface unsaturated zone and the deep saturated zone. Evaporation-induced hypersalinity has been measured at multiple coastal sites, including sand beaches in Delaware Bay and the Gulf of Mexico (Geng & Boufadel, 2017; Geng et al., 2016), as well as wetlands in the Northern Gulf of California (Glenn et al., 2006; Morzaria-Luna et al., 2014). However, the combined impacts of evaporation and waves on subsurface flow and salinity dynamics in the swash zone remain inadequately explored. This is likely because direct field measurements through discrete sampling points cannot fully capture the highly dynamic nature of these processes, especially for the influence of waves, and numerical modeling is lacking. Nevertheless, understanding these dynamics is crucial for comprehending various aspects of beach systems, including subsurface biogeochemical transformation, contaminant fate, and ecosystem functionality.

The objective of this research is to investigate the combined mechanisms driving salinity dynamics in the swash zone, influenced by evaporation and high-frequency breaking waves. Using numerical simulations and field measurements, we aim to elucidate the synergistic effects of waves and evaporation on subsurface flow and salt transport in shallow beach environments. This study examines the alternating impacts of evaporation and wave infiltration on the temporal and spatial evolution of subsurface pore-water flow and salinity distribution in the swash zone, under varying sediment and atmospheric conditions.

2. Methodology

2.1. Field Work Conducted in Heiss et al. (2015)

Field measurements were conducted at Herring Point, Cape Henlopen, DE, USA, on a sandy (0.39 mm median grain size) beach. Within the swash zone, a transect of six instrument arrays were deployed, each containing 5 moisture sensors (Decagon Device EC-5) installed at 4- to 6-cm depth intervals, ranging from 2 cm below the sand surface to a maximum depth of 24 cm. These deployed moisture sensors were used to measure fluctuations in moisture content in response to swash motions. Pressure transducers (Druck PTX 1835) were mounted to each instrument array to capture the effects of wave-induced high-frequency pressure oscillations at the sand surface. These transducers recorded surface water pressure variations, allowing us to determine when the transect was inundated by swash. Additionally, Druck PTX 1835 transducers were installed under the moisture sensors in the saturated zone to capture saturated pore pressure and water table response to tide and swash forcing across the beach surface. Tides were semidiurnal with a mean tidal range of 1.4 m. Further details regarding the field

19447973, 2024, 11, Downloaded from https://agupubs.onlinelibrary.wiley.com/doi/10.1029/2024WR037427, Wiley Online Library on [26/11/2024]. See the Terms and Conditions (https://onlinelibrary.wiley.com/terms-and-conditions) on Wiley Online Library for rules of use; OA articles are governed by the applicable Creative Commons License

19447973, 2024, 11, Downloaded from https://agupubs.onlinelibrary.wiley.com/doi/10.1029/2024WR037427, Wiley Online Library on [26/11/2024]. See the Terms and Conditions (https://onlinelibrary.wiley.com/terms-and-conditions) on Wiley Online Library for rules of use; OA articles are governed by the applicable Creative Commons License

Table 1
Model Parameter Values Used in the Numerical Simulations

Symbol	Definition	Units	Value
α	Capillary fringe parameter of the van Genuchten [1980] model	m^{-1}	5.0
n	Sand grain size distribution parameter of the van Genuchten [1980] model	-	7.9
K_0	Saturated freshwater hydraulic conductivity	ms^{-1}	2.4×10^{-4}
α_L	Longitudinal dispersivity	m	0.04
α_T	Transverse dispersivity	m	0.004
ξ	Fitting parameter of density concentration relationship	lg^{-1}	7.44×10^{-4}
S_0	Specific storage	m^{-1}	10^{-5}
S_r	Residual soil saturation	-	0.1
Φ	Porosity	-	0.37
CONVP	The convergence criterion of pressure head in the Picard iterative scheme of MARUN code	m	10^{-5}
τD_m	Product of tortuosity and diffusion coefficient	m^2s^{-1}	10^{-9}

measurements are shown in Figure S1 of Supporting Information S1, which can also be found in Heiss et al. (2015).

2.2. Groundwater Flow and Solute Transport Model

Subsurface flow and solute transport were simulated using the variably saturated density-dependent model MARUN (Boufadel et al., 1999; Geng & Boufadel, 2015c, 2017; Li et al., 2008). The simulated domain represented a 2-D cross-section of a beach aquifer, measuring 2.5 m in length and varying in depth from 6.76 to 6.26 m depending on the beach topography, extending horizontally from the landward to seaward instrument arrays (Figure 1). The mesh resolution was approximately 5 cm in the horizontal direction and about 2 cm above and 5 cm below elevation $z = 0$ in the vertical direction. The water table observed from the most landward and seaward pressure transducers was assigned as the landward and seaward boundary conditions for flow, respectively. Pressure data measured by the transducers at the sand surface were interpolated across the transect and assigned to each surface node to represent the swash forcing. A freshwater salinity of 0.0 g/L was assigned at the landward boundary. The model performed a check on the surface nodes: a Dirichlet boundary condition of 35.0 g/L was assigned for the nodes where seawater infiltrated, and a Cauchy boundary condition was assigned to the nodes exposed to the air. The simulations were run for 144 hr with observed semidiurnal tidal cycles until the hydraulic and salinity distribution reached a quasi-steady state. The time step was automatically adjusted by the model to ensure convergence criteria were met (Courant number <1). This site-specific numerical model has undergone extensive validation in our earlier research on groundwater dynamics in the swash zone, both for homogeneous and heterogeneous sediments (Geng et al., 2017, 2020), where evaporation effects are not taken into account. The parameter values used for the simulations are reported in Table 1.

2.3. Evaporation

Evaporation occurred on the portion of the surface exposed to the air. A Neumann boundary condition was adopted on the sand surface to simulate evaporated water flow, and the evaporation flux, E_g, was calculated using the bulk aerodynamic approach (Mahfouf & Noilhan, 1991):

$$E_g = \frac{\rho_{air}}{\rho_{water} R_{air}} (q_g - q_{air}). \quad (1)$$

Here, ρ_{air} and ρ_{water} represent the density of air and freshwater, 1.1839 kg/m^3 and 1.0×10^3 kg/m^3, respectively, q_a and q_g are the air and surface relative humidity, and R_{air} is the aerodynamic resistance, expressed as $94.909 \times u^{-0.9036}$, where u represents the wind speed at the atmospheric reference level (~2 m above the soil surface), given in Table 2. A Cauchy boundary condition was adopted in the MARUN model to simulate solute accumulation below the soil surface due to evaporation, expressed as follows (Geng & Boufadel, 2015a):

19447973, 2024, 11, Downloaded from https://agupubs.onlinelibrary.wiley.com/doi/10.1029/2024WR037427, Wiley Online Library on [26/11/2024]. See the Terms and Conditions (https://onlinelibrary.wiley.com/terms-and-conditions) on Wiley Online Library for rules of use; OA articles are governed by the applicable Creative Commons License

Table 2
Simulated Cases With Model Parameter Values

Case	Evaporation	K (m/s)	α (1/m)	Temperature (°C)	Relative humidity (−)	Wind speed (m/s)
1	No	2.4×10^{-4}	5.0	-	-	-
2	Yes	2.4×10^{-4}	5.0	17	60% (day), 80% (night)	2.2
3	Yes	2.4×10^{-4}	5.0	22	40% (day), 80% (night)	4.47
4	Yes	2.4×10^{-4}	5.0	27	20% (day), 80% (night)	8.94
5	No	9.6×10^{-5}	2.0	-	-	-
6	Yes	9.6×10^{-5}	2.0	17	60% (day), 80% (night)	2.2
7	Yes	9.6×10^{-5}	2.0	22	40% (day), 80% (night)	4.47
8	Yes	9.6×10^{-5}	2.0	27	20% (day), 80% (night)	8.94
9	No	4.8×10^{-5}	1.0	-	-	-
10	Yes	4.8×10^{-5}	1.0	17	60% (day), 80% (night)	2.2
11	Yes	4.8×10^{-5}	1.0	22	40% (day), 80% (night)	4.47
12	Yes	4.8×10^{-5}	1.0	27	20% (day), 80% (night)	8.94

$$\left(\vec{q}c - \beta\phi SD \cdot \nabla c\right) \cdot \vec{n} = 0, \tag{2}$$

Here $\vec{q}$ is the Darcy flux vector, c is the solute concentration, β is the density ratio between actual water density to freshwater density, ϕ is the porosity of the porous medium, S is the soil moisture, D represents the physical dispersion tensor, $\vec{n}$ is the vector normal to the boundary.

In this study, we simulated three meteorological conditions to represent typical summer climates with dry, intermediate dry, and humid conditions where the field data were collected (Lewes, Delaware, USA). The sediment properties, such as hydraulic conductivity and capillarity, are expected to strongly impact the evaporation from the beach surface. Therefore, we also included three sediment properties, assuming a linear correlation between the thickness of the capillary fringe ($1/\alpha$) and hydraulic conductivity (K), following the approach by von Jeetze et al. (2020):

$$\frac{K_1}{K_0} = (1 + 0.1R_N)\frac{\alpha_1}{\alpha_0}, \tag{3}$$

Here K_i and α_i are the hydraulic conductivity and the inverse of the air-entry value, the latter of which represents an estimate of the thickness of the capillary fringe, $i = 0, 1$ are the two sediment types considered, and R_N is a uniformly distributed random variable between 0 and 1, accounting for certain perturbation of the correlation. We also conducted simulations without evaporation for comparison. All of the simulated cases are summarized in Table 2.

3. Results

3.1. Wave-Evaporation-Induced Increase in Salinity

Wave motion generates a saline plume beneath the swash zone, with hypersalinity (salinity >45.0 g/L) near the surface being triggered by evaporation under certain sediment and atmospheric conditions (Figure 2). Swash-driven infiltration of seawater leads to the formation of a saline plume beneath the swash zone. Notably, in cases of high permeability, this plume does not extend downward below the water table appreciably, particularly after the waves have receded seaward of the model domain (Cases 1–4). This occurs because high permeability within the swash zone facilitates groundwater discharge, which in turn flushes the saline plume seaward once saturated conditions facilitate horizontal flow. In cases with intermediate to low permeability, the saline plume extends beneath the water table (Cases 5–12). Under dry atmospheric conditions, a hypersaline layer forms near the beach surface (Cases 4, 8, 12), and evaporation induces an upwelling of groundwater toward the swash zone

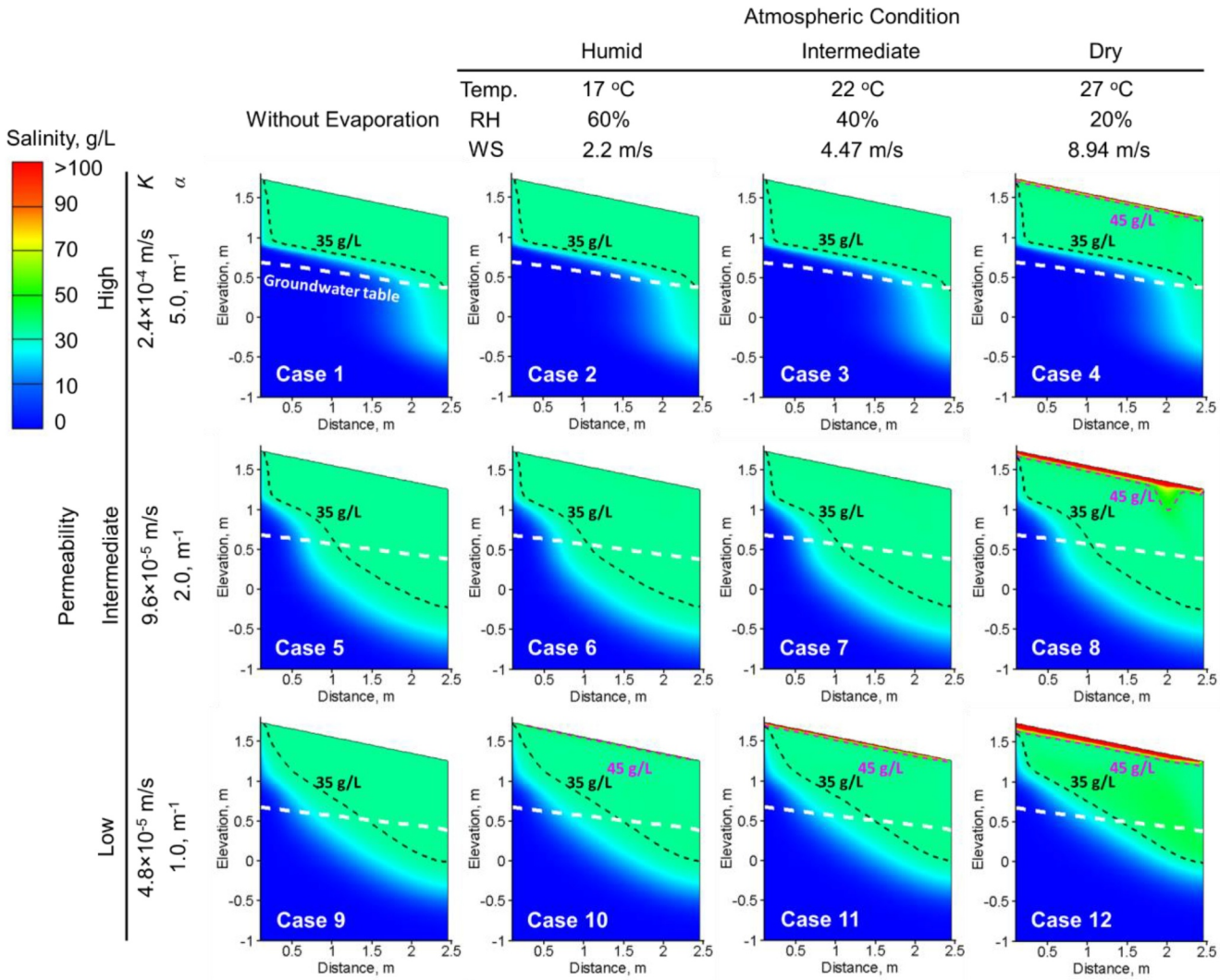

Figure 2. Salinity distribution for Cases 1–12 simulated under different hydraulic and atmospheric conditions, highlighting the time $t = 16$ hr when the highest salinity is observed at the surface.

surface. This occurs because evaporation accumulates salt in the near-surface pore spaces, increasing salinity above seawater concentration in the upper decimeter of the beach. In relatively low-permeability cases (Cases 9–12), evaporative-driven upward movement of low-salinity groundwater is restricted. This limits the dilution of accumulated salt by deep low-salinity groundwater, leading to very high pore water salinities. In those same low-permeability cases, a relatively high capillary fringe along with dry atmospheric conditions creates a high humidity gradient, which in turn intensifies the evaporation rate. These factors collectively contribute to hypersalinity near the surface.

3.2. Temporal Evolution of Evaporation Rate, Moisture Content, and Salinity

Wave motion induces dynamic changes in the evaporation rate, altering the near-surface salinity in the swash zone. The simulation results from Case 8 (medium permeability and dry conditions) demonstrate that high-frequency waves acting on the swash zone cause significant fluctuations in the evaporation rate (Figures 3a and 3b). Wave runup motion inundates the swash zone, temporarily halting evaporation while increasing the water content within the near-surface sediments. Conversely, wave run-down motion exposes these high-moisture sediments to the air, promoting evaporation on the swash zone's surface. However, as the swash zone recedes seaward during falling tide, there is a substantial decrease in the evaporation rate over time, corresponding to the

19447973, 2024, 11, Downloaded from https://agupubs.onlinelibrary.wiley.com/doi/10.1029/2024WR037427, Wiley Online Library on [26/11/2024]. See the Terms and Conditions (https://onlinelibrary.wiley.com/terms-and-conditions) on Wiley Online Library for rules of use; OA articles are governed by the applicable Creative Commons License

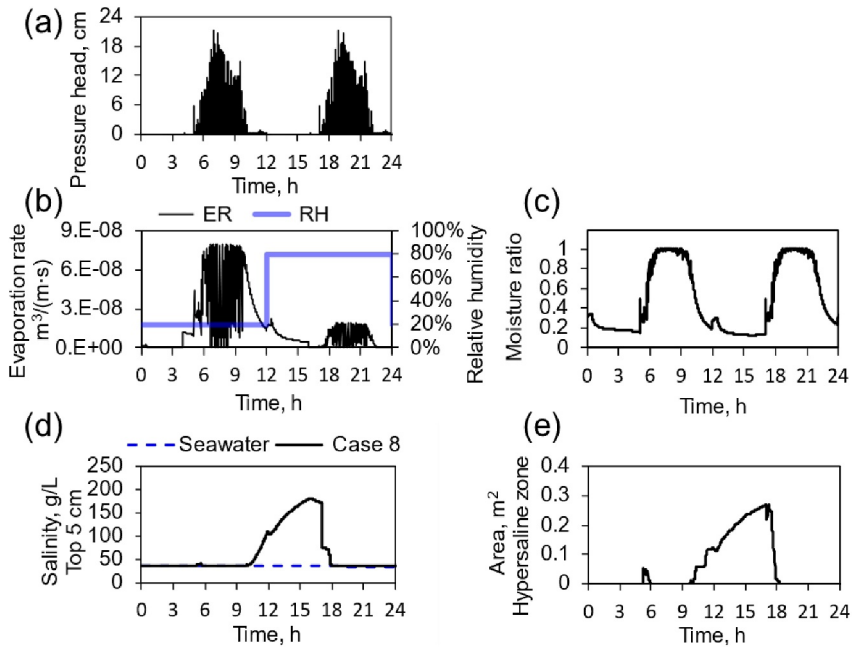

Figure 3. Simulation results from Case 8 ($K = 9.6 \times 10\text{-}5$ m/s, temperature = 27°C, wind speed (WS) = 8.97 m/s, and relative humidity (RH) = 20% (day) and 80% (night)). Temporal evolution of (a) swash-induced pressure oscillation measured at the beach surface by the pressure transducer deployed at $x = 2.08$ m, (b)–(c) average evaporation rate (ER) and moisture ratio along the swash zone, (d) average salinity within the top 5 cm sediment layer of the swash zone, and (e) the cross-sectional areal extent of the hypersaline zone where salinity> 45 g/L for Case 8.

decline in surface moisture at the sand surface (Figures 3b and 3c). Additionally, there is an apparent inconsistency between the increase in evaporation rates and the salinity at the swash zone's surface. During periods of high fluctuation in the evaporation rate, specifically between times $t = 5.0$ and 10.0 hr (Figure 3b), the near-surface salinity does not exceed that of seawater (Figure 3d). This is likely due to the rapid dilution of accumulated salt by the seawater infiltration following wave inundation. However, the average salinity within the top 5 cm of sediment significantly increases after the swash zone recedes during falling tide (Figure 3d). During this period the salinity in the upper 5 cm increases from that of seawater to nearly 200 g/L, indicating substantial salt accumulation even as the evaporation rate gradually drops. The temporal evolution of the hypersaline zone area also reflects these distinct patterns: the spatial extent of the hypersaline plume increases due to evaporation without wave overtopping (Figure 3e). Salinity in the upper 5 cm returns to seawater salinity at $t = 18$ hr when the rising tide lifts the swash zone higher onto the beach, leading to seawater infiltration and dilution of hypersalinity pore water (Figure 3d). These results highlight the competing effects of waves and evaporation on altering near-surface salinity along the swash zone.

3.3. Evolution of Evaporation-Induced Hypersaline Plume

The interaction between waves and evaporation drives a complex spatial evolution of the hypersaline plume beneath the swash zone. The simulation results from Case 8 demonstrate the following dynamics: during periods of wave recession, when the swash zone moves seaward during falling tide, evaporation leads to increased salt accumulation at the exposed beach surface, resulting in the formation of a hypersaline plume in the subsurface (Figures 4a and 4b). This hypersaline plume notably expands at the seaward portion of the swash zone. When waves begin impacting the hypersaline zone, the subsurface hypersaline plume becomes diluted with seawater and is pushed landward and downward (Figures 4c and 4d). Consequently, the hypersaline zone is only observed at the upper portion of the swash zone, where swash inundation is minimal (Figure 4e). This dynamic interaction leads to spatial variation in salinity along the swash zone over time (Figure 4f). In the absence of waves, the near-surface salinity along the simulated beach portion, especially at its lower seaward side, remains relatively high. Conversely, as the swash zone moves onto the simulated sand surface there is a gradual decrease in the near-

19447973, 2024, 11, Downloaded from https://agupubs.onlinelibrary.wiley.com/doi/10.1029/2024WR037427, Wiley Online Library on [26/11/2024]. See the Terms and Conditions (https://onlinelibrary.wiley.com/terms-and-conditions) on Wiley Online Library for rules of use; OA articles are governed by the applicable Creative Commons License

19447973, 2024, 11, Downloaded from https://agupubs.onlinelibrary.wiley.com/doi/10.1029/2024WR037427, Wiley Online Library on [26/11/2024]. See the Terms and Conditions (https://onlinelibrary.wiley.com/terms-and-conditions) on Wiley Online Library for rules of use; OA articles are governed by the applicable Creative Commons License

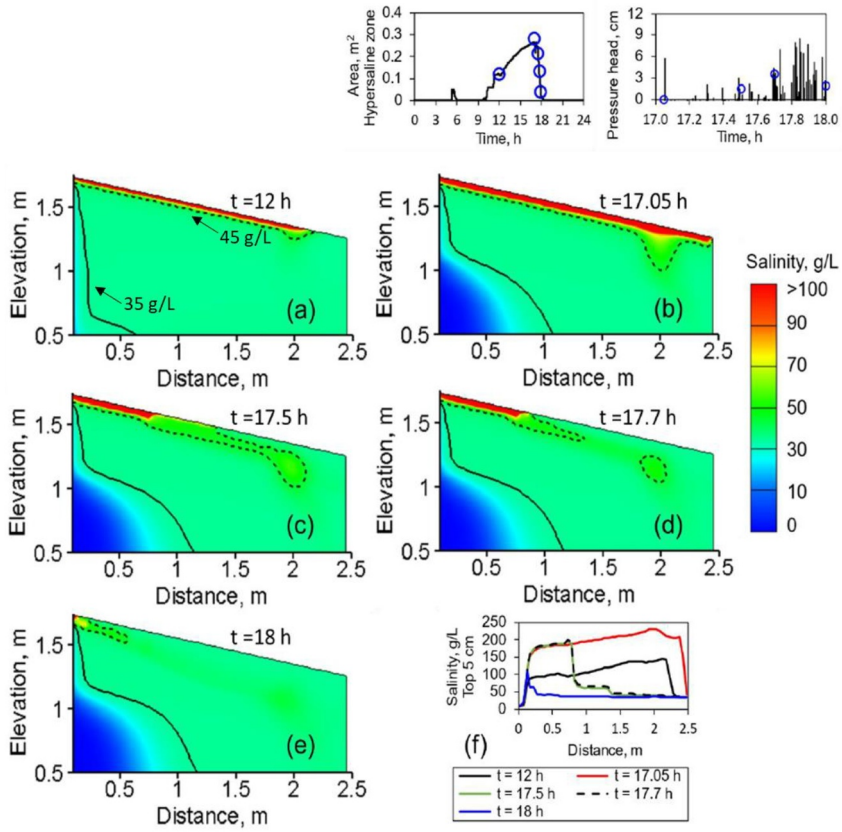

Figure 4. (a–e) Case 8 salinity distribution at times t = 12 hr, 17.05 hr, 17.5 hr, 17.7 hr, and 18 hr along the swash zone when a hypersaline plume develops due to evaporation. (f) Average salinity within the top 5 cm sediment layer at these times. The dashed black lines in the contour plots delineate the hypersaline zone (salinity >45 g/L), and solid black lines represent the saline zone with salinity above seawater salinity (35 g/L). The areal extent of the hypersaline zone and the swash-induced pressure oscillation, previously shown in Figure 2, are provided in the rightmost panel, with the time points selected for salinity contour marked as circle symbols.

surface salinity at the swash front due to the dilution; therefore, relatively high salinity appears at the upper landward portion of the simulated beach surface.

3.4. Soil Moisture Distribution

Wave motion leads to dynamic changes in moisture conditions within the swash zone, which are strongly correlated to salinity, as shown in the comparison between Figures 4 and 5, using Case 8 as an example. When the swash zone is seaward of the model domain, the moisture ratio is higher near the lower part of the simulated sand surface due to more frequent inundation by wave-induced seawater infiltration (Figures 5a and 5b). This elevated moisture accounts for the higher salinity levels observed in this area, as it sustains a relatively high rate of evaporation on the surface. As wave overtopping occurs at t = 17 hr, seawater infiltration at the swash front increases the moisture ratio to form a tongue of saturated sediment (Figures 5c and 5d). This influx of saltwater dilutes the accumulated salt at these locations (Figures 4c and 4d; Figures 5c and 5d). As a result, the hypersaline zone recedes further landward due to swash motion.

3.5. Spatial Distribution of Evaporation Rate Along the Swash Zone

Wave motion alters both the spatial extent and the rate of evaporation along the swash zone (Figure 6a). The variation in the spatial extent of evaporation corresponds to the temporal fluctuation of the overall evaporation rate along the swash zone. This correlation suggests that in the presence of waves, the intensity of evaporation along the swash zone is significantly governed by its changing spatial extent. The spatial distribution of evaporation rates along the swash zone, at various stages of wave propagation toward the landward side, shows a

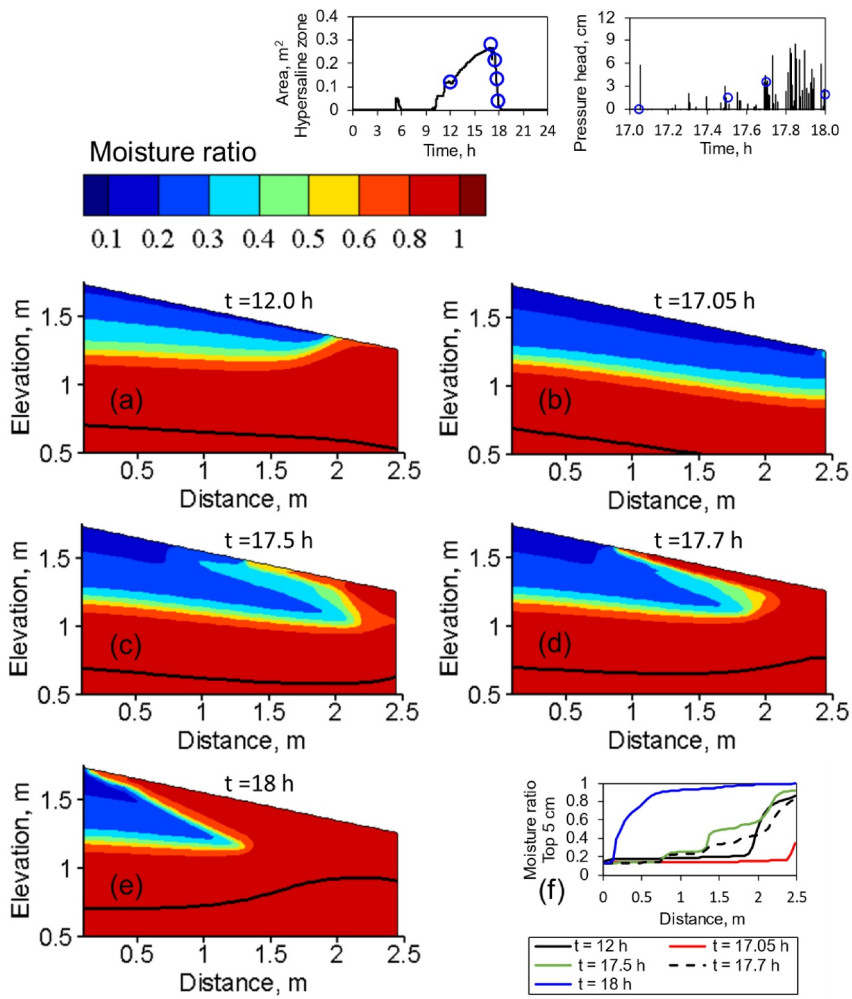

Figure 5. (a–e) Moisture ratio distribution at times t = 12 hr, 17.05 hr, 17.5 hr, 17.7 hr, and 18 hr along the swash zone when an apparent hypersaline plume develops due to evaporation in Case 8. (f) Average moisture ratio within the top 5 cm sediment layer at these times. The black lines in the contour plots represent the groundwater table.

relatively consistent rate within the area where evaporation occurs (Figures 6b–6d). This consistency is attributed to the near-saturated sediments at the surface, which maintain a stable humidity gradient conducive to evaporation. Consequently, the overall evaporation rate is determined by this spatially uniform rate, factored by the spatial extent of evaporation along the swash zone. In contrast, as waves recede seaward of the swash zone, the near-surface moisture becomes a crucial factor in limiting the overall evaporation rate (Figures 6e–6g). During the period of wave recession, such as at time t = 10, 13, and 15 hr, evaporation occurs along the entire swash zone but at varying rates. Notably, higher evaporation rates of 7.76×10^{-8} $m^3/(m{\cdot}s)$, 3.44×10^{-8} $m^3/(m{\cdot}s)$, and 1.72×10^{-8} $m^3/(m{\cdot}s)$ are observed toward the seaward side at time t = 10, 13, 15 hr, respectively, corresponding to the increased moisture in that area, compared to the rates of 3.37×10^{-8} $m^3/(m{\cdot}s)$, 1.86×10^{-9} $m^3/(m{\cdot}s)$, and 1.05×10^{-9} $m^3/(m{\cdot}s)$ simulated at the landward side.

3.6. Penetration Depth of Evaporation-Induced Hypersaline Plume

Waves and evaporation recursively impact the development of the hypersaline plume beneath the swash zone. As shown in Figure 7a the migration depth of the hypersaline plume in Case 8 varies with the periodic motion of waves, reaching its maximum depth during periods of wave recession. On average, the plume extends to a depth of 10 cm, with a maximum simulated depth of 30 cm (Figure 7a). The evaporation-induced hypersalinity at the modeled sand surface creates vertical density gradients, which facilitate the expansion of the hypersaline plume

19447973, 2024, 11, Downloaded from https://agupubs.onlinelibrary.wiley.com/doi/10.1029/2024WR037427, Wiley Online Library on [26/11/2024]. See the Terms and Conditions (https://onlinelibrary.wiley.com/terms-and-conditions) on Wiley Online Library for rules of use; OA articles are governed by the applicable Creative Commons License

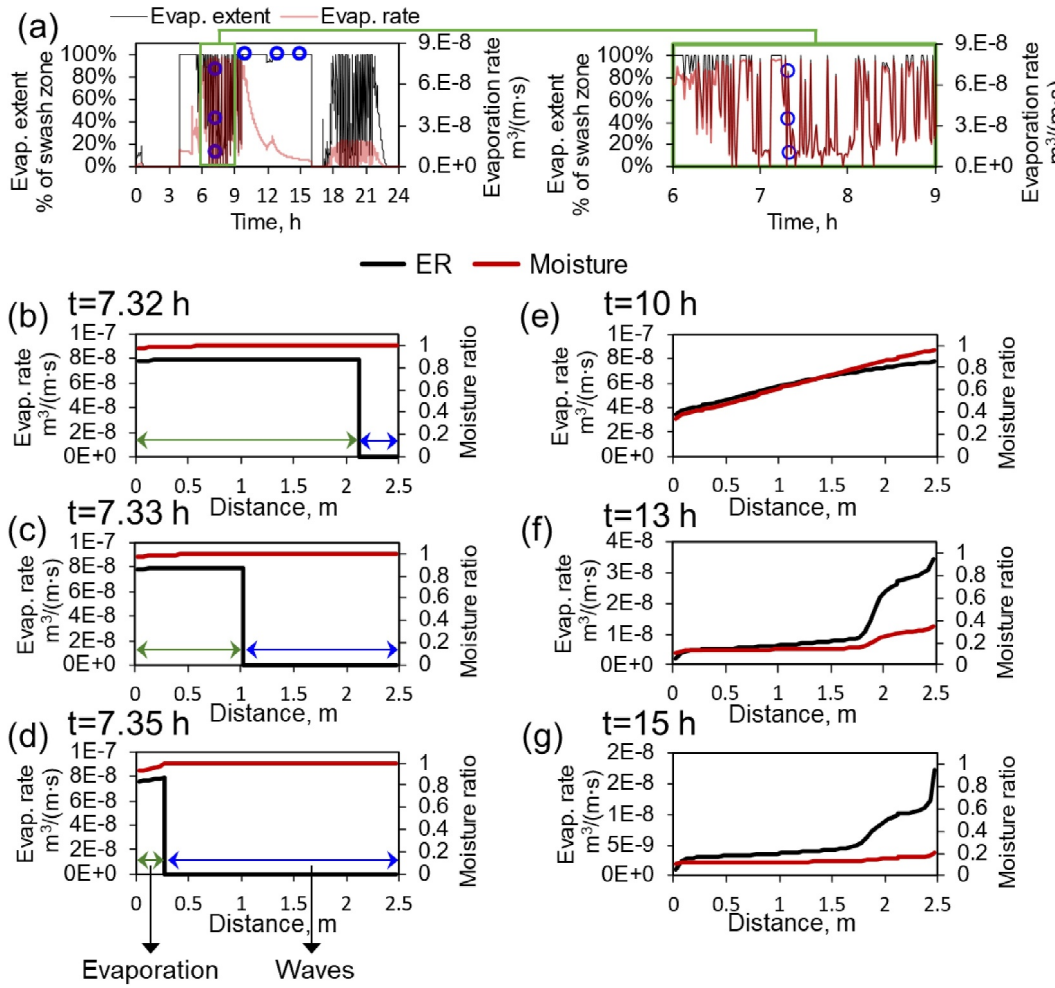

Figure 6. (a) Temporal evolution of evaporation spatial extent (% of swash zone) in Case 8. (b–g) Spatial distribution of evaporation rate along the swash zone surface at times marked as blue circles in panel (a).

into deeper sediments. The vertical salinity profiles show a significant decrease in salinity with increasing depth (Figure 7b). Notably, at times t = 12, 14, and 16 hr, the salinity near the swash zone surface nearly approaches its solubility limit but then decreases rapidly to below 40 g/L within a 20 cm depth. This pattern indicates that although salinity is extremely high near the surface, the accumulated mass of salt is relatively low compared to the broader volume of surrounding saline water. This difference allows for rapid dilution, effectively preventing the formation of a persistent hypersaline plume in the deep sediments beneath the swash zone.

3.7. Comparison of Evaporation and Salinity Across Simulation Cases

Evaporation along the swash zone is significantly influenced by both sediment properties and atmospheric conditions. The no-evaporation cases simulated with varying permeabilities show distinct moisture conditions on the beach surface (Figure 8a). In sediments with low permeability, a relatively high capillary fringe contributes to a higher moisture near the swash zone. Notably, in Case 9 (lowest permeability), the beach surface remains saturated between individual swash events and sustains levels above 60% when swash zone shifts seaward during low tide. In contrast, in the higher permeability cases (Cases 1 and 5), moisture fluctuates with wave action on the swash zone and rapidly decreases to nearly residual levels after the waves recede. This is likely because higher permeability facilitates the drainage of infiltrating seawater within the unsaturated zone, and a relatively low capillary fringe does not sustain high moisture near the surface. The evaporation extent exhibits distinct temporal patterns across the swash zone in sediments of varying permeabilities. In cases with high and intermediate K, the spatial extent of evaporation decreases as surface moisture drops, eventually reducing to zero when the moisture

19447973, 2024, 11, Downloaded from https://agupubs.onlinelibrary.wiley.com/doi/10.1029/2024WR037427, Wiley Online Library on [26/11/2024]. See the Terms and Conditions (https://onlinelibrary.wiley.com/terms-and-conditions) on Wiley Online Library for rules of use; OA articles are governed by the applicable Creative Commons License

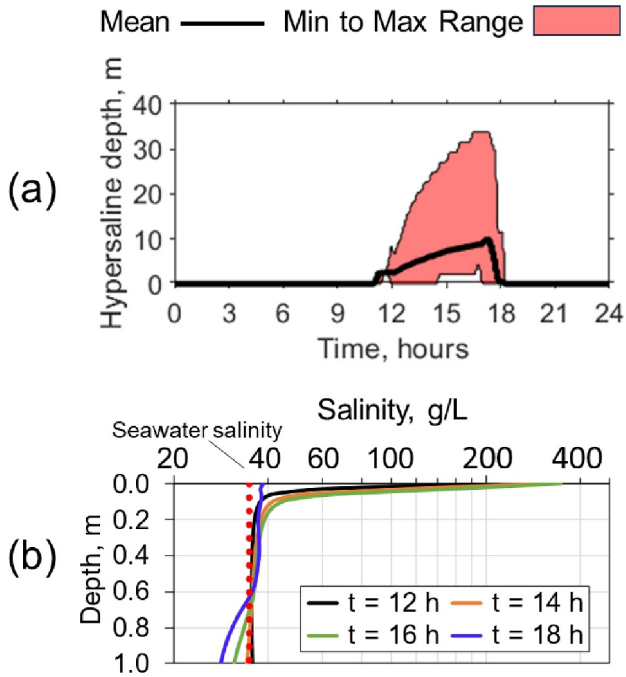

Figure 7. Hypersaline plume depth in the swash zone for Case 8. (a) Temporal evolution of hypersaline depth. (b) Vertical distribution of salinity, representing the horizontal average at each depth at times t = 12 hr, 14 hr, 16 hr, and 18 hr.

ratio drops below the threshold necessary for evaporation to occur under specific atmospheric conditions (Figures 8b and 8c). These temporal patterns indicate that high sediment permeability reduces surface moisture, thereby limiting evaporation and the associated salt accumulation near the swash zone surface. In contrast, in all low-permeability cases (Cases 10–12), the spatial extent of evaporation covers the entire simulated beach portion under various atmospheric conditions, indicating adequate water content on the surface to trigger evaporation (Figure 8d). However, the overall evaporation rate reveals that atmospheric conditions are crucial in controlling the evaporation rate. The overall evaporation from the swash zone shows higher rates with increasingly dry atmospheric conditions (Figure 8e). Once there is sufficient water content on the surface to support evaporation, the actual rate of evaporation is primarily governed by humidity gradients, which are, in turn, determined by moisture as well as atmospheric conditions.

Optimal hydrogeological and atmospheric conditions interact to maximize salt accumulation near the surface of the swash zone through evaporation. A boxplot of salinity within the top 5 cm of the sediments reveals higher salinity levels in the cases simulated under dry atmospheric conditions (Figure 9a). This is expected, as dry atmospheric conditions are likely to generate larger humidity gradients and higher evaporation rates, thereby facilitating salt accumulation along the swash zone surface. Interestingly, salinity is most elevated in Case 8 with intermediate K and dry atmospheric conditions, rather than in cases with high K. This phenomenon occurs because, in high-permeability sediments, increased hydraulic conductivity leads to a lower capillary fringe and to moisture-limited conditions at the sand surface. These factors attenuate evaporation over periods of wave recession and subsequent salt accumulation. Conversely, in low-permeability sediments, the high moisture content within the unsaturated zone enhances mixing and exchange between the evaporation-induced hypersaline zone near the surface and the deeper sediments containing relatively low-salinity water, thereby limiting salt accumulation near the swash zone surface. Therefore, intermediate-K sediments present optimal conditions for salt accumulation along the swash zone through evaporation. Importantly, these results show that while the highest evaporation occurs in Case 12, the most pronounced increase in salinity is observed in Case 8. This pattern indicates that the increase in salinity is not exclusively correlated with evaporation, emphasizing the

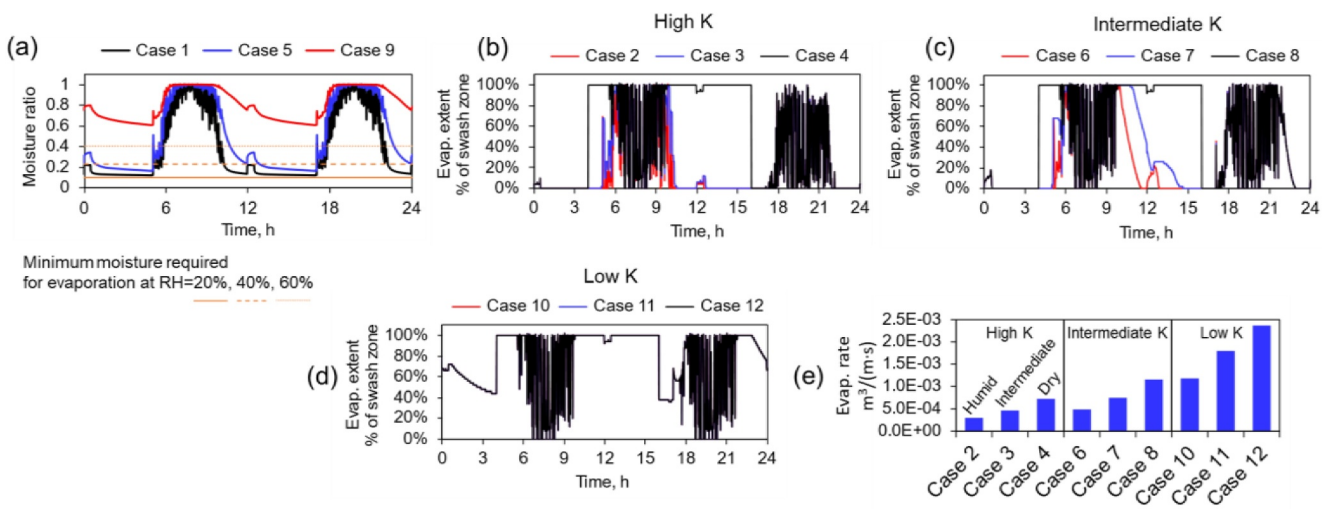

Figure 8. (a) Temporal evolution of average moisture ratio along the swash zone surface for noevaporation cases. (b–d) Temporal evolution of evaporation extent for (a) high K (Cases 2–4), (b) intermediate K (Cases 6–8), and (c) low K (Cases 10–12) evaporation cases. (e) Total evaporation rate along the swash zone over a tidal cycle for all evaporation cases (Cases 2–12). Individual plots of the evaporation extent for each case are shown in Figure S3 of Supporting Information S1.

19447973, 2024, 11, Downloaded from https://agupubs.onlinelibrary.wiley.com/doi/10.1029/2024WR037427, Wiley Online Library on [26/11/2024]. See the Terms and Conditions (https://onlinelibrary.wiley.com/terms-and-conditions) on Wiley Online Library for rules of use; OA articles are governed by the applicable Creative Commons License

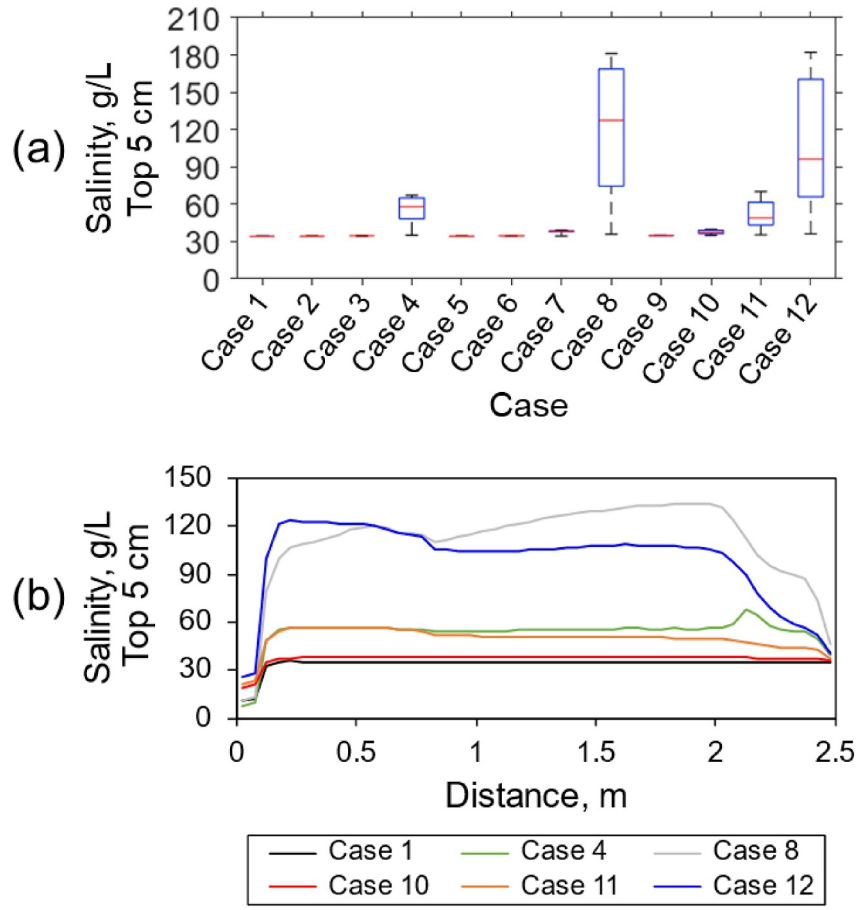

Figure 9. (a) Salinity comparison within the top 5 cm sediment layer in the swash zone for periods when salt accumulation occurs (e.g., between time t = 10 and 18 hr). (b) Spatial distribution of average salinity within the top 5 cm sediment layer over 12 hr for cases showing apparent salinity increase (Cases 4, 8, and 10–12) compared to the no evaporation case (Case 1). In panel (a), each boxplot summarizes the median (line inside the box), interquartile range (box), and data range (whiskers).

significant role of sediment properties in regulating salinity changes along the swash zone. The spatial distribution of salinity varies along the swash zone under different sediment and atmospheric conditions (Figure 9b). The average salinity within the top 5 cm of the sediment layer over 12 hr demonstrates relatively high salinity levels at the upper portions of the swash zone x = 0–1.0 m in all cases where a hypersaline plume is present. Salt accumulation is facilitated near the upper portion of the swash zone where swash inundation is infrequent and there is ample time for evaporation (Figure 9b).

The salinity and size of the hypersaline zone varies temporally and spatially under the sediment and atmospheric conditions tested. As shown in Figures 10a and 10b, the hypersaline plume in Case 12 (high-K and dry conditions) is the largest in size and penetrates the deepest into sediments over the 24 hr simulation period. This larger spatial extent is attributed to the higher water content within the unsaturated zone in this low-K scenario, which allows for the vertical expansion of the hypersaline plume. Additionally, the average salinity within the hypersaline plume in Case 12 is the highest, except for a specific period between time from t = 10–14 hr when the salinity is higher in Case 8 (intermediate-K and dry conditions (Figure 10c). This phenomenon can be attributed to the high moisture content in Case 12 between time t = 10–14 hr, which mitigates the increase in salinity within the hypersaline zone by diluting it with deeper, low-salinity groundwater. Conversely, during other periods, the low moisture content in the remaining simulated cases prohibits salt accumulation due to limited evaporation rates. The results indicate the presence of optimal moisture levels conducive to salt accumulation near the surface. Above these moisture levels, the hypersaline plume can be rapidly diluted by the surrounding low-salinity groundwater as the plume spreads downwards. Conversely, below these levels, an increase in salinity is impeded by low or zero evaporation on the swash zone surface. Additionally, the boxplot of average salinity

19447973, 2024, 11, Downloaded from https://agupubs.onlinelibrary.wiley.com/doi/10.1029/2024WR037427, Wiley Online Library on [26/11/2024]. See the Terms and Conditions (https://onlinelibrary.wiley.com/terms-and-conditions) on Wiley Online Library for rules of use; OA articles are governed by the applicable Creative Commons License

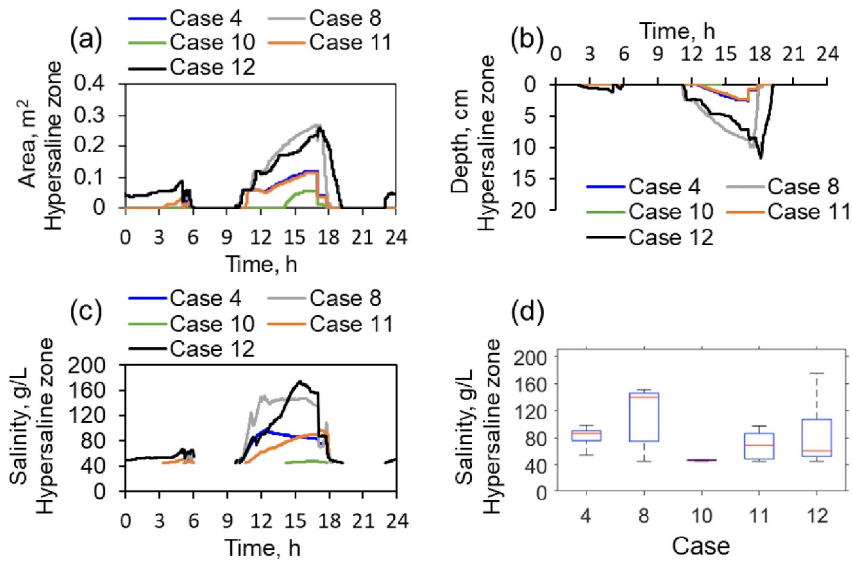

Figure 10. (a) Temporal evolution of average salinity within the hypersaline zone. (b) Salinity comparison within the hypersaline zone for cases where hypersaline zone develops. (c–d) Temporal evolution of areal extent and average depth of hypersaline zone in the swash zone. The boxplot shown in panel (b) summarizes the median (line inside the box), interquartile range (box), and data range (whiskers).

levels shows that Case 12 exhibits the greatest temporal variation in salinity (Figure 10d). This large variation is a result of the plume's prolonged presence within the swash zone, subjected to significant accumulation and dilution over swash cycles. These results highlight the complex development of the hypersaline plume and its substantial variation in salinity and geometry.

4. Discussion

Our study highlights the dynamic changes in salinity within the swash zone, governed by the combined effects of wave action and evaporation. In particular, under certain sediment and atmospheric conditions, evaporation triggers hypersalinity at the surface of the swash zone, which then migrates downwards due to vertical density and hydraulic gradients. The salinity of pore water is crucial to the functioning and ecological services of beach environments (Drouin et al., 1985; Javanshir, 2013; Kinne, 1971). For example, shallow beach environments are essential for the hatching and nesting of various coastal species such as sea turtles and birds (Koch et al., 2007; Maslo et al., 2016; Stewart et al., 2018). Elevated salt concentration can lead to cellular dehydration, reduced turgor pressure, and impaired embryonic development (Aladin, 1991; Einav et al., 2003; Nabavi et al., 2013). Chaudhary et al. (2023) observed a significant decrease in microbial and enzyme activities in hypersaline benthic environments. Previous research also indicates that hypersalinity hampers the microbially mediated uptake of dissolved organic carbon (DOC) and dissolved organic nitrogen (DON) (Paerl & Yannarell, 2010; Pinckney et al., 1995; Yannarell & Paerl, 2007). Additionally, as climate change alters spatial and temporal patterns of evaporation and intensifies drought events, it will increase the likelihood of hypersalinity occurring due to the combined impacts of evaporation and waves in coastal zones. Therefore, the temporal and spatial changes in salinity in the swash zone, as revealed in our study, could have profound implications for biogeochemical processes in coastal beach ecosystems.

In coastal marine sediments, the supralittoral and sublittoral zones are recognized as being particularly vulnerable to nearshore oil spills (Boufadel et al., 2014; Geng et al., 2015; Huettel et al., 2018). A notable example is the Deepwater Horizon oil spill, which released approximately 3.19 million barrels (510 million liters) of crude oil into the Gulf of Mexico (GOM). Despite considerable efforts to prevent the oil from reaching the Gulf shorelines, hundreds of kilometers of coastlines along the northern GOM were contaminated (Boufadel et al., 2023). The landward transport of the spilled oil, predominantly driven by currents and waves, resulted in oil being buried as deep as half a meter deep in sandy beaches. Studies have shown that subsurface oil contamination from such spills can persist in beach sediments for years or even decades (Bernabeu et al., 2009; Boufadel et al., 2019). The

19447973, 2024, 11, Downloaded from https://agupubs.onlinelibrary.wiley.com/doi/10.1029/2024WR037427, Wiley Online Library on [26/11/2024]. See the Terms and Conditions (https://onlinelibrary.wiley.com/terms-and-conditions) on Wiley Online Library for rules of use; OA articles are governed by the applicable Creative Commons License

19447973, 2024, 11, Downloaded from https://agupubs.onlinelibrary.wiley.com/doi/10.1029/2024WR037427, Wiley Online Library on [26/11/2024]. See the Terms and Conditions (https://onlinelibrary.wiley.com/terms-and-conditions) on Wiley Online Library for rules of use; OA articles are governed by the applicable Creative Commons License

primary mechanism for the natural removal of oil contaminants within these sediments is biodegradation. Studies have demonstrated that hypersalinity, a critical environmental factor, significantly impedes the microbial degradation of weathered oil in marine sediments (Abou Khalil et al., 2021; Geng, Khalil, et al., 2021). Therefore, the insights provided here on the salinity dynamics of the swash zone are essential for assessing the persistence of oil and for developing effective mitigation strategies on beaches impacted by oil spills. In our study, we used a salinity level of 35.0 g/L for coastal waters, based on field measurements at the study site. However, in certain coastal regions such as estuaries, lagoons, and areas with significant submarine groundwater discharge, the intensive mixing of terrestrial fresh groundwater with seawater reduces salinity near the shoreline. To account for this, we simulated a scenario with coastal water salinity at 25.0 g/L, while keeping the meteorological conditions consistent with those of Case 8. The results indicate that hypersalinity can occur even in coastal zones with initially lower salinity levels under specific meteorological conditions (Figure S2 in Supporting Information S1). This suggests the mechanisms driving hypersalinity revealed in this paper could be prevalent in a wide range of coastal zones.

Our study simulates complex atmosphere−ocean−beach interactions along the swash zone, which modulate water flux and solute exchange across the land-sea interface. These findings have significant implications for monitoring and investigating surface evaporation and groundwater salinity in coastal zones. Waves increase near-surface moisture, leading to an elevated evaporation rate, accompanied by dynamic fluctuations due to high-frequency surface inundation caused by individual waves. This indicates that the swash zone is a hotspot for evaporation to occur along the coasts. Additionally, the dynamic patterns simulated in this study suggest a need for high temporal and spatial resolution measurements to accurately quantify the overall evaporation rate along the swash zone. Our results also demonstrate that the highest evaporation intensity does not necessarily result in the greatest salt concentrations within the swash zone. This finding implies that salt accumulation in the swash zone is not exclusively correlated with surface evaporation but also depends on subsurface hydrogeological conditions. Therefore, comprehensive measurements, integrating both surface and subsurface data, are essential for characterizing salinity changes in the swash zone. Furthermore, evaporation-induced hypersalinity at the swash zone emerges under specific sediment and atmospheric conditions, which might not be ubiquitously observed in the field.

5. Conclusion

Simulations of coastal groundwater flow and salt transport reveal that wave motion generates a saline plume beneath the swash zone, with hypersalinity near the surface being triggered by intensified evaporation. Waves increase moisture content near the beach surface, leading to increased evaporation rates, which fluctuate due to high-frequency surface inundation driven by swash motion. The interaction between swash inundation and evaporation drives a complex spatial evolution of the hypersaline plume beneath the swash zone. During periods of wave recession, evaporation leads to salt accumulation at the swash zone surface. This results in the formation of a hypersaline plume beneath the swash zone that expands downwards, driven by vertical density gradients. As waves start to impact the hypersaline zone, the hypersaline plume is pushed both landward and downwards due to wave-induced seawater infiltration, and it is subsequently diluted by the surrounding saline groundwater. The downward expansion of this hypersaline plume is confined to a depth of about 30 cm, likely due to the relatively low accumulated mass of salt compared to the volume of surrounding low-salinity groundwater.

Our study demonstrates that the highest evaporation intensity on the swash zone surface does not necessarily lead to the greatest salt accumulation within the swash zone. Simulation results under identical atmospheric conditions show that the highest evaporation rates occur in low-permeability sediments, while the most pronounced salt accumulation is observed in sediments of intermediate permeability. This is because in very high-permeability sediments, a lower capillary fringe leads to moisture-limited conditions at the swash zone surface and thus low evaporation, and the increased hydraulic conductivity facilitates wave-induced seawater infiltration that dilutes hypersaline pore water. Conversely, in very low-permeability sediments, the high capillary fringe enhances mixing between the surface's evaporation-induced hypersaline zone and the deeper low-salinity pore water, thereby limiting salt accumulation near the swash zone surface. The capillary fringe in sediments of intermediate permeability is high enough to supply moisture to the sand surface for evaporation, and simultaneously low enough to limit mixing between the shallow hypersaline pore water and lower-salinity pore water at depth. This finding indicates that optimal sediment properties exist to maximize salt accumulation near the swash zone surface through evaporation. These insights are important for obtaining a better understanding of coastal

groundwater flow, biogeochemical conditions, and consequent nutrient cycling and contaminant transport in coastal zones, highlighting the necessity of considering integrated coastal physical and atmospheric drivers when investigating coastal flow and transport processes in coastal swash zones.

Data Availability Statement

Modeling files along with data supporting this study are from HydroShare (Geng, 2024).

Acknowledgments
This work was funded by the US NSF (EAR2130595 and CBET2345629). However, it does not necessarily reflect the views of the funding agency, and no official endorsement should be inferred. This is SOEST contribution #11863.

References

Abou Khalil, C., Fortin, N., Prince, R. C., Greer, C. W., Lee, K., & Boufadel, M. C. (2021). Crude oil biodegradation in upper and supratidal seashores. *Journal of Hazardous Materials*, *416*, 125919. https://doi.org/10.1016/j.jhazmat.2021.125919

Abou Khalil, C., Prince, V. L., Prince, R. C., Greer, C. W., Lee, K., Zhang, B., & Boufadel, M. C. (2020). Occurrence and biodegradation of hydrocarbons at high salinities. *Science of the Total Environment*, *762*, 143165. https://doi.org/10.1016/j.scitotenv.2020.143165

Aladin, N. V. (1991). Salinity tolerance and morphology of the osmoregulation organs in Cladocera with special reference to Cladocera from the Aral Sea. *Hydrobiologia*, *225*, 291–299. https://doi.org/10.1007/978-94-017-0918-7_28

Anwar, N., Robinson, C., & Barry, D. A. (2014). Influence of tides and waves on the fate of nutrients in a nearshore aquifer: Numerical simulations. *Advances in Water Resources*, *73*, 203–213. https://doi.org/10.1016/j.advwatres.2014.08.015

Armonies, W. (1988). Physical factors influencing active emergence of meiofauna from boreal intertidal sediment. *Marine Ecology Progress Series. Oldendorf*, *49*, 277–286. https://doi.org/10.3354/meps049277

Atherton, R. J., Baird, A. J., & Wiggs, G. F. (2001). Inter-tidal dynamics of surface moisture content on a meso-tidal beach. *Journal of Coastal Research*, 482–489.

Bakhtyar, R., Brovelli, A., Barry, D. A., & Li, L. (2011). Wave-induced water table fluctuations, sediment transport and beach profile change: Modeling and comparison with large-scale laboratory experiments. *Coastal Engineering*, *58*(1), 103–118. https://doi.org/10.1016/j.coastaleng.2010.08.004

Bernabeu, A. M., Rey, D., Rubio, B., Vilas, F., Domínguez, C., Bayona, J. M., & Albaigés, J. (2009). Assessment of cleanup needs of oiled sandy beaches: Lessons from the prestige oil spill. *Environmental Science and Technology*, *43*(7), 2470–2475. https://doi.org/10.1021/es803209h

Boufadel, M., Geng, X., An, C., Owens, E., Chen, Z., Lee, K., et al. (2019). A review on the factors affecting the deposition, retention, and biodegradation of oil stranded on beaches and guidelines for designing laboratory experiments. *Current Pollution Reports*, *5*(4), 407–423. https://doi.org/10.1007/s40726-019-00129-0

Boufadel, M. C., Abdollahi-Nasab, A., Geng, X., Galt, J., & Torlapati, J. (2014). Simulation of the landfall of the deepwater Horizon oil on the shorelines of the Gulf of Mexico. *Environmental Science and Technology*, *48*(16), 9496–9505. https://doi.org/10.1021/es5012862

Boufadel, M. C., Li, H., Suidan, M. T., & Venosa, A. D. (2007). Tracer studies in a laboratory beach subjected to waves. *Journal of Environmental Engineering*, *133*(7), 722–732. https://doi.org/10.1061/(asce)0733-9372(2007)133:7(722)

Boufadel, M. C., Özgökmen, T., Socolofsky, S. A., Kourafalou, V. H., Liu, R., & Lee, K. (2023). Oil transport following the Deepwater Horizon blowout. *Annual Review of Marine Science*, *15*(1), 67–93. https://doi.org/10.1146/annurev-marine-040821-104411

Boufadel, M. C., Suidan, M. T., & Venosa, A. D. (1999). A numerical model for density-and-viscosity-dependent flows in two-dimensional variably saturated porous media. *Journal of Contaminant Hydrology*, *37*(1–2), 1–20. https://doi.org/10.1016/s0169-7722(98)00164-8

Chambers, L. G., Guevara, R., Boyer, J. N., Troxler, T. G., & Davis, S. E. (2016). Effects of salinity and inundation on microbial community structure and function in a mangrove peat soil. *Wetlands*, *36*(2), 361–371. https://doi.org/10.1007/s13157-016-0745-8

Charbonnier, C., Anschutz, P., Poirier, D., Bujan, S., & Lecroart, P. (2013). Aerobic respiration in a high-energy sandy beach. *Marine Chemistry*, *155*, 10–21. https://doi.org/10.1016/j.marchem.2013.05.003

Chaudhary, D. R., Kumar, M., & Kalla, V. (2023). Sediment microbial community structure, enzymatic activities and functional gene abundance in the coastal hypersaline habitats. *Archives of Microbiology*, *205*(2), 56. https://doi.org/10.1007/s00203-022-03398-4

Cockcroft, A. (1990). Nitrogen excretion by the surf zone bivalves Donax serra and D. sordidus. *Marine Ecology Progress Series. Oldendorf*, *60*, 57–65. https://doi.org/10.3354/meps060057

Drouin, G., Himmelman, J. H., & Béland, P. (1985). Impact of tidal salinity fluctuations on echinoderm and mollusc populations. *Canadian Journal of Zoology*, *63*(6), 1377–1387. https://doi.org/10.1139/z85-207

Einav, R., Harussi, K., & Perry, D. (2003). The footprint of the desalination processes on the environment. *Desalination*, *152*(1–3), 141–154. https://doi.org/10.1016/s0011-9164(02)01057-3

Geng, X. (2024). Influence of evaporation and high-frequency seawater inundation on salinity dynamics in swash zones [Dataset]. *HydroShare*. https://doi.org/10.4211/hs.774abdf009a54b358d35e501eca34fd8

Geng, X., & Boufadel, M. C. (2015a). Numerical modeling of water flow and salt transport in bare saline soil subjected to evaporation. *Journal of Hydrology*, *524*, 427–438. https://doi.org/10.1016/j.jhydrol.2015.02.046

Geng, X., & Boufadel, M. C. (2015b). Numerical study of solute transport in shallow beach aquifers subjected to waves and tides. *Journal of Geophysical Research: Oceans*, *120*(2), 1409–1428. https://doi.org/10.1002/2014jc010539

Geng, X., & Boufadel, M. C. (2015c). Impacts of evaporation on subsurface flow and salt accumulation in a tidally influenced beach. *Water Resources Research*, *51*(7), 5547–5565. https://doi.org/10.1002/2015wr016886

Geng, X., & Boufadel, M. C. (2017). The influence of evaporation and rainfall on supratidal groundwater dynamics and salinity structure in a sandy beach. *Water Resources Research*, *53*(7), 6218–6238. https://doi.org/10.1002/2016wr020344

Geng, X., Boufadel, M. C., & Jackson, N. L. (2016). Evidence of salt accumulation in beach intertidal zone due to evaporation. *Scientific Reports*, *6*(1), 31486. https://doi.org/10.1038/srep31486

Geng, X., Boufadel, M. C., Lee, K., Abrams, S., & Suidan, M. (2015). Biodegradation of subsurface oil in a tidally influenced sand beach: Impact of hydraulics and interaction with pore water chemistry. *Water Resources Research*, *51*(5), 3193–3218. https://doi.org/10.1002/2014wr016870

Geng, X., Boufadel, M. C., Li, H., Na Nagara, V., & Lee, K. (2023). Impacts of evaporation-induced groundwater upwelling on mixing dynamics in shallow wetlands. *Geophysical Research Letters*, *50*(15), e2023GL104642. https://doi.org/10.1029/2023GL104642

Geng, X., Boufadel, M. C., Xia, Y., Li, H., Zhao, L., Jackson, N. L., & Miller, R. S. (2014). Numerical study of wave effects on groundwater flow and solute transport in a laboratory beach. *Journal of Contaminant Hydrology*, *165*, 37–52. https://doi.org/10.1016/j.jconhyd.2014.07.001

Geng, X., Heiss, J. W., Michael, H. A., & Boufadel, M. C. (2017). Subsurface flow and moisture dynamics in response to swash motions: Effects of beach hydraulic conductivity and capillarity. *Water Resources Research*, *53*(12), 10317–10335. https://doi.org/10.1002/2017wr021248

19447973, 2024, 11, Downloaded from https://agupubs.onlinelibrary.wiley.com/doi/10.1029/2024WR037427, Wiley Online Library on [26/11/2024]. See the Terms and Conditions (https://onlinelibrary.wiley.com/terms-and-conditions) on Wiley Online Library for rules of use; OA articles are governed by the applicable Creative Commons License

Geng, X., Heiss, J. W., Michael, H. A., Boufadel, M. C., & Lee, K. (2020). Groundwater flow and moisture dynamics in the swash zone: Effects of heterogeneous hydraulic conductivity and capillarity. *Water Resources Research*, *56*(11), e2020WR028401. https://doi.org/10.1029/2020WR028401

Geng, X., Heiss, J. W., Michael, H. A., Li, H., Raubenheimer, B., & Boufadel, M. C. (2021). Geochemical fluxes in sandy beach aquifers: Modulation due to major physical stressors, geologic heterogeneity, and nearshore morphology. *Earth-Science Reviews*, *221*, 103800. https://doi.org/10.1016/j.earscirev.2021.103800

Geng, X., Khalil, C. A., Prince, R. C., Lee, K., An, C., & Boufadel, M. C. (2021). Hypersaline pore water in Gulf of Mexico beaches prevented efficient biodegradation of deepwater Horizon beached oil. *Environmental Science and Technology*, *55*(20), 13792–13801. https://doi.org/10.1021/acs.est.1c02760

Glenn, E. P., Nagler, P. L., Brusca, R. C., & Hinojosa-Huerta, O. (2006). Coastal wetlands of the northern Gulf of California: Inventory and conservation status. *Aquatic Conservation: Marine and Freshwater Ecosystems*, *16*(1), 5–28. https://doi.org/10.1002/aqc.681

Heiss, J. W., Michael, H. A., & Puleo, J. A. (2020). Groundwater-surface water exchange in the intertidal zone detected by hydrologic and coastal oceanographic measurements. *Hydrological Processes*, *34*(17), 3718–3721. https://doi.org/10.1002/hyp.13825

Heiss, J. W., Puleo, J. A., Ullman, W. J., & Michael, H. A. (2015). Coupled surface-subsurface hydrologic measurements reveal infiltration, recharge, and discharge dynamics across the swash zone of a sandy beach. *Water Resources Research*, *51*(11), 8834–8853. https://doi.org/10.1002/2015wr017395

Heiss, J. W., Ullman, W. J., & Michael, H. A. (2014). Swash zone moisture dynamics and unsaturated infiltration in two sandy beach aquifers. *Estuarine, Coastal and Shelf Science*, *143*, 20–31. https://doi.org/10.1016/j.ecss.2014.03.015

Hirt, C. W., & Nichols, B. D. (1981). Volume of fluid (VOF) method for the dynamics of free boundaries. *Journal of Computational Physics*, *39*(1), 201–225. https://doi.org/10.1016/0021-9991(81)90145-5

Horn, D. P. (2006). Measurements and modelling of beach groundwater flow in the swash-zone: A review. *Continental Shelf Research*, *26*(5), 622–652. https://doi.org/10.1016/j.csr.2006.02.001

Huettel, M., Overholt, W. A., Kostka, J. E., Hagan, C., Kaba, J., Wells, W. B., & Dudley, S. (2018). Degradation of Deepwater Horizon oil buried in a Florida beach influenced by tidal pumping. *Marine Pollution Bulletin*, *126*, 488–500. https://doi.org/10.1016/j.marpolbul.2017.10.061

Huizer, S., Karaoulis, M. C., Oude Essink, G. H. P., & Bierkens, M. F. P. (2017). Monitoring and simulation of salinity changes in response to tide and storm surges in a sandy coastal aquifer system. *Water Resources Research*, *53*(8), 6487–6509. https://doi.org/10.1002/2016wr020339

Javanshir, A. (2013). How salinity changes in an intertidal zone may affect population dynamics of Littorina scabra (Linaeus 1758) in northern coasts of Persian Gulf. *Turkish Journal of Fisheries and Aquatic Sciences*, *13*(1). https://doi.org/10.4194/1303-2712-v13_1_17

Kim, K. H., & Heiss, J. W. (2021). Methods in capturing the spatiotemporal dynamics of flow and biogeochemical reactivity in sandy beach aquifers: A review. *Water*, *13*(6), 782. https://doi.org/10.3390/w13060782

Kinne, O. (1971). Salinity-invertebrates. *Marine Ecology*.

Koch, A. U., Guinea, M. L., & Whiting, S. D. (2007). Effects of sand erosion and current harvest practices on incubation of the flatback sea turtle (Natator depressus). *Australian Journal of Zoology*, *55*(2), 97. https://doi.org/10.1071/ZO06063

Lew, S., Glińska-Lewczuk, K., Burandt, P., Kulesza, K., Kobus, S., & Obolewski, K. (2022). Salinity as a determinant structuring microbial communities in coastal lakes. *International Journal of Environmental Research and Public Health*, *19*(8), 4592. https://doi.org/10.3390/ijerph19084592

Li, H., Boufadel, M. C., & Weaver, J. W. (2008). Tide-induced seawater–groundwater circulation in shallow beach aquifers. *Journal of Hydrology*, *352*(1–2), 211–224. https://doi.org/10.1016/j.jhydrol.2008.01.013

Li, H., Li, L., & Lockington, D. (2005). Aeration for plant root respiration in a tidal marsh. *Water Resources Research*, *41*(6). https://doi.org/10.1029/2004wr003759

Liu, Y., Zhang, C., Liu, X., Li, C., Sheuermann, A., Xin, P., et al. (2022). Salt transport under tide and evaporation in a subtropical wetland: Field monitoring and numerical simulation. *Water Resources Research*, *58*(5), e2021WR031530. https://doi.org/10.1029/2021wr031530

Longuet-Higgins, M., & Smith, N. (1983). Measurement of breaking waves by a surface jump meter. *Journal of Geophysical Research*, *88*(C14), 9823–9831. https://doi.org/10.1029/jc088ic14p09823

Longuet-Higgins, M. S. (1983). Wave set-up, percolation and undertow in the surf zone. *Proceedings of the Royal Society of London. A. Mathematical and Physical Sciences*, *390*, 283–291.

Mahfouf, J., & Noilhan, J. (1991). Comparative study of various formulations of evaporations from bare soil using in situ data. *Journal of Applied Meteorology*, *30*(9), 1354–1365. https://doi.org/10.1175/1520-0450(1991)030<1354:csovfo>2.0.co;2

Maslo, B., Schlacher, T. A., Weston, M. A., Huijbers, C. M., Anderson, C., Gilby, B. L., et al. (2016). Regional drivers of clutch loss reveal important trade-offs for beach-nesting birds. *PeerJ*, *4*, e2460. https://doi.org/10.7717/peerj.2460

Moore, W. S., & Joye, S. B. (2021). Saltwater intrusion and submarine groundwater discharge: Acceleration of biogeochemical reactions in changing coastal aquifers. *Frontiers in Earth Science*, *9*, 600710. https://doi.org/10.3389/feart.2021.600710

Morgan, S. G., Shanks, A. L., MacMahan, J. H., Reniers, A. J., & Feddersen, F. (2018). Planktonic subsidies to surf-zone and intertidal communities. *Annual Review of Marine Science*, *10*(1), 345–369. https://doi.org/10.1146/annurev-marine-010816-060514

Morzaria-Luna, H., Turk-Boyer, P., Rosemartin, A., & Camacho-Ibar, V. F. (2014). Vulnerability to climate change of hypersaline salt marshes in the Northern Gulf of California. *Ocean and Coastal Management*, *93*, 37–50. https://doi.org/10.1016/j.ocecoaman.2014.03.004

Mouret, A., Charbonnier, C., Lecroart, P., Metzger, E., Howa, H., Deflandre, B., et al. (2020). Biogeochemistry in an intertidal pocket beach. *Estuarine, Coastal and Shelf Science*, *243*, 106920. https://doi.org/10.1016/j.ecss.2020.106920

Nabavi, S. M. B., Miri, M., Doustshenas, B., Safahieh, A. R., & Loghmani, M. (2013). Effects of a brine discharge over bottom polychaeta community structure in Chabahar bay. *Journal of Life Sciences*, *7*, 302.

Paerl, H. W., & Yannarell, A. C. (2010). Environmental dynamics, community structure and function in a hypersaline microbial mat. *Microbial Mats: Modern and Ancient Microorganisms in Stratified Systems*, 421–442. https://doi.org/10.1007/978-90-481-3799-2_22

Pinckney, J., Paerl, H. W., & Bebout, B. M. (1995). Salinity control of benthic microbial mat community production in a Bahamian hypersaline lagoon. *Journal of Experimental Marine Biology and Ecology*, *187*(2), 223–237. https://doi.org/10.1016/0022-0981(94)00185-g

Robinson, C., Xin, P., Li, L., & Barry, D. A. (2014). Groundwater flow and salt transport in a subterranean estuary driven by intensified wave conditions. *Water Resources Research*, *50*(1), 165–181. https://doi.org/10.1002/2013wr013813

Silvestri, S., Defina, A., & Marani, M. (2005). Tidal regime, salinity and salt marsh plant zonation. *Estuarine, Coastal and Shelf Science*, *62*(1–2), 119–130. https://doi.org/10.1016/j.ecss.2004.08.010

Sous, D., Lambert, A., Rey, V., & Michallet, H. (2013). Swash–groundwater dynamics in a sandy beach laboratory experiment. *Coastal Engineering*, *80*, 122–136. https://doi.org/10.1016/j.coastaleng.2013.05.006

Sous, D., Petitjean, L., Bouchette, F., Rey, V., Meulé, S., Sabatier, F., & Martins, K. (2016). Field evidence of swash groundwater circulation in the microtidal roustty beach, France. *Advances in Water Resources*, *97*, 144–155. https://doi.org/10.1016/j.advwatres.2016.09.009

19447973, 2024, 11, Downloaded from https://agupubs.onlinelibrary.wiley.com/doi/10.1029/2024WR037427, Wiley Online Library on [26/11/2024]. See the Terms and Conditions (https://onlinelibrary.wiley.com/terms-and-conditions) on Wiley Online Library for rules of use; OA articles are governed by the applicable Creative Commons License

Steenhauer, K., Pokrajac, D., O'Donoghue, T., & Kikkert, G. A. (2011). Subsurface processes generated by bore-driven swash on coarse-grained beaches. *Journal of Geophysical Research*, *116*(C4), C04013. https://doi.org/10.1029/2010jc006789

Stewart, T. A., Booth, D. T., & Rusli, M. U. (2018). Influence of sand grain size and nest microenvironment on incubation success, hatchling morphology and locomotion performance of green turtles (Chelonia mydas) at the Chagar Hutang Turtle Sanctuary, Redang Island, Malaysia. *Australian Journal of Zoology*, *66*(6), 356. https://doi.org/10.1071/ZO19025

Turner, I. L., Rau, G. C., Austin, M. J., & Andersen, M. S. (2016). Groundwater fluxes and flow paths within coastal barriers: Observations from a large-scale laboratory experiment (BARDEX II). *Coastal Engineering*, *113*, 104–116. https://doi.org/10.1016/j.coastaleng.2015.08.004

Uchiyama, Y., Nadaoka, K., Rölke, P., Adachi, K., & Yagi, H. (2000). Submarine groundwater discharge into the sea and associated nutrient transport in a sandy beach. *Water Resources Research*, *36*(6), 1467–1479. https://doi.org/10.1029/2000wr900029

von Jeetze, P. J., Zarebanadkouki, M., & Carminati, A. (2020). Spatial heterogeneity enables higher root water uptake in dry soil but protracts water stress after transpiration decline: A numerical study. *Water Resources Research*, *56*(1), e2019WR025501. https://doi.org/10.1029/2019wr025501

Wang, Y., Huang, Q., Lemckert, C., & Ma, Y. (2017). Laboratory and field magnetic evaluation of the heavy metal contamination on Shilaoren Beach, China. *Marine Pollution Bulletin*, *117*(1–2), 291–301. https://doi.org/10.1016/j.marpolbul.2017.01.080

Wilcox, D. C. (1993). *Turbulence modeling*. DCW Industries.

Wilcox, D. C. (1998). *Turbulence modeling for CFD*. DCW industries La Canada.

Xin, P., Robinson, C., Li, L., Barry, D. A., & Bakhtyar, R. (2010). Effects of wave forcing on a subterranean estuary. *Water Resources Research*, *46*(12). https://doi.org/10.1029/2010wr009632

Xin, P., Zhou, T., Lu, C., Shen, C., Zhang, C., D'Alpaos, A., & Li, L. (2017). Combined effects of tides, evaporation and rainfall on the soil conditions in an intertidal creek-marsh system. *Advances in Water Resources*, *103*, 1–15. https://doi.org/10.1016/j.advwatres.2017.02.014

Yannarell, A. C., & Paerl, H. W. (2007). Effects of salinity and light on organic carbon and nitrogen uptake in a hypersaline microbial mat. *FEMS Microbiology Ecology*, *62*(3), 345–353. https://doi.org/10.1111/j.1574-6941.2007.00384.x

Zeppilli, D., Leduc, D., Fontanier, C., Fontaneto, D., Fuchs, S., Gooday, A. J., et al. (2018). Characteristics of meiofauna in extreme marine ecosystems: A review. *Marine Biodiversity*, *48*(1), 35–71. https://doi.org/10.1007/s12526-017-0815-z

Zhang, C., Li, L., & Lockington, D. (2014). Numerical study of evaporation-induced salt accumulation and precipitation in bare saline soils: Mechanism and feedback. *Water Resources Research*, *50*(10), 8084–8106. https://doi.org/10.1002/2013wr015127

19447973, 2024, 11, Downloaded from https://agupubs.onlinelibrary.wiley.com/doi/10.1029/2024WR037427, Wiley Online Library on [26/11/2024]. See the Terms and Conditions (https://onlinelibrary.wiley.com/terms-and-conditions) on Wiley Online Library for rules of use; OA articles are governed by the applicable Creative Commons License